Surface Plasmonic Effects of Metallic Nanoparticles on the Performance of Polymer Bulk Heterojunction Solar Cells

Jyh-Lih Wu,[†] Fang-Chung Chen,[‡,]* Yu-Sheng Hsiao,[§] Fan-Ching Chien,[§] Peilin Chen,[§] Chun-Hong Kuo,[⊥] Michael H. Huang,[⊥] and Chain-Shu Hsu[∥]

[†]Department of Photonics and Institute of Electro-optical Engineering, National Chiao Tung University, Hsinchu 30010, Taiwan, [‡]Department of Photonics and Display Institute, National Chiao Tung University, Hsinchu 30010, Taiwan, [§]Research Center for Applied Sciences, Academia Sinica, Taipei 11529, Taiwan, [⊥]Department of Chemistry, National Tsing Hua University, Hsinchu 3001, Taiwan, and [∥]Department of Applied Chemistry, National Chiao Tung University, Hsinchu 30010, Taiwan

Organic photovoltaic devices (OPVs) are promising alternative tools for harnessing renewable energy because of their properties including lightweight, low-cost, low-temperature fabrication, semi-transparency, and mechanical flexibility. To date, the most representative high-performance OPVs reported in the literature have been fabricated using the bulk heterojunction (BHJ) concept,[1−6] where a light-absorbing polymer (donor) and a soluble fullerene (acceptor) form a three-dimensional matrix possessing a large-area phase-separated interface for efficient exciton dissociation.[7,8] The resultant power conversion efficiencies (PCEs) of these polymer/fullerene BHJ OPV devices have reached as high as 6−8%,[1−4] opening up the possibility for their practical use as flexible, low-cost, renewable energy systems. As a result, increasing effort is being exerted in the quest for higher-performance OPVs.

The overall efficiency of an OPV device is governed by its internal quantum efficiency and absorption efficiency.[9,10] The former, which is influenced by the diffusion and dissociation of photogenerated excitons and charge collection at the electrode contacts, can approach 100%.[3] Therefore, absorption efficiency of incoming light in these devices remains one of the major limitations toward realizing high external quantum efficiencies and PCEs. Typically, the optimum thickness of the active layer for an OPV device is on the order of 100−200 nm, or possibly less; such a thin layer can lead to low absorption of light. Therefore, increasing the thickness of the active layer is one possible approach toward

ABSTRACT We have systematically explored how plasmonic effects influence the characteristics of polymer photovoltaic devices (OPVs) incorporating a blend of poly(3-hexylthiophene) (P3HT) and [6,6]-phenyl-C_{61}-butyric acid methyl ester (PCBM). We blended gold nanoparticles (Au NPs) into the anodic buffer layer to trigger localized surface plasmon resonance (LSPR), which enhanced the performance of the OPVs without dramatically sacrificing their electrical properties. Steady state photoluminescence (PL) measurements revealed a significant increase in fluorescence intensity, which we attribute to the increased light absorption in P3HT induced by the LSPR. As a result, the rate of generation of excitons was enhanced significantly. Furthermore, dynamic PL measurements revealed that the LSPR notably reduced the lifetime of photogenerated excitons in the active blend, suggesting that interplay between the surface plasmons and excitons facilitated the charge transfer process. This phenomenon reduced the recombination level of geminate excitons and, thereby, increased the probability of exciton dissociation. Accordingly, both the photocurrents and fill factors of the OPV devices were enhanced significantly. The primary origin of this improved performance was local enhancement of the electromagnetic field surrounding the Au NPs. The power conversion efficiency of the OPV device incorporating the Au NPs improved to 4.24% from a value of 3.57% for the device fabricated without Au NPs.

KEYWORDS: polymer photovoltaics · gold nanoparticles · surface plasmon · photoluminescence · exciton lifetime

more efficient light absorption. A thicker layer, however, inevitably increases the device resistance, due to the low carrier mobilities and short exciton diffusion lengths of organic materials.[11,12] This situation imposes a trade-off between light absorption and charge transport efficiencies in OPV devices, motivating the development of a variety of light-trapping techniques.

Efficient light trapping in the active layer enhances photon absorption without the need for a thick film. The introduction of an optical spacer that spatially redistributes the light intensity in the device can result in enhanced light absorption.[13−16] Changes in
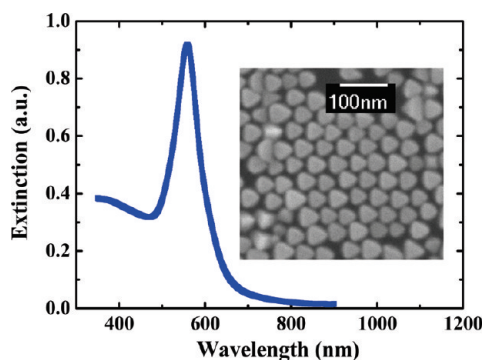
Figure 1. UV–vis extinction spectrum of the solution-processable Au NPs. Inset: Corresponding SEM image. Average Au NP size = *ca.* 45 ± 5 nm.
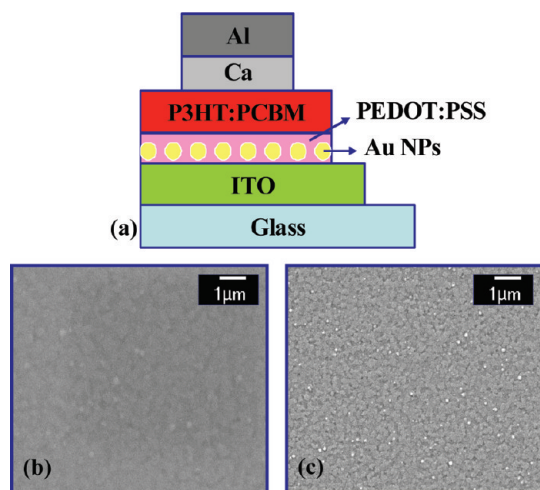

Figure 2. (a) Device architecture of the OPV incorporating Au NPs in the PEDOT:PSS layer. (b,c) SEM images of anodic buffer layers prepared with (b) pristine PEDOT:PSS and (c) PEDOT:PSS featuring embedded Au NPs. The Au NPs appear as white dots in (c).

the device symmetry and the implementation of periodic nanostructures can also increase the optical path length in the active layer.[17−20] Moreover, microcavity and photonic crystal effects have been proposed to effectively trap light in OPV devices.[21−23]

Recently, the exploitation of surface plasmon resonance (SPR) effects, based on advantageous optical properties such as light concentration and/or scattering, has attracted much attention as a means for increasing the photocurrents of OPVs.[24−32] Two primary schemes are commonly employed for excitation of the SPR, which is the coherent collective oscillation of conduction electrons surrounding the metallic surfaces. In one, surface plasmon polaritons (SPPs) propagating along the metal–dielectric interface are triggered by incorporating metallic nanostructures, such as periodic arrays or gratings.[24−26] In the other, surface plasmons are localized by noble metallic nanoparticles (NPs)—such as Cu, Ag, Pt, and Au—resulting in localized surface plasmon resonance (LSPR).[27−32] The excitation of LSPR can be achieved

when the frequency of the incident light matches its resonance peak, resulting in unique optical properties—selective light extinction as well as local enhancement of electromagnetic field near the surface of metallic NPs. The resonance peak of LSPR depends strongly on the size, shape, and the dielectric environment of the metallic NPs. Although both approaches have been employed to increase the photocurrents of OPV devices, a comprehensive understanding of such plasmonic effects in OPVs remains rare. In this study, we systematically explored how plasmonic effects influence the device characteristics of OPVs incorporating a blend of poly(3-hexylthiophene) (P3HT) and [6,6]-phenyl-C_{61}-butyric acid methyl ester (PCBM). Excitation of the LSPR—triggered by adding Au NPs into the anodic buffer layer—significantly enhanced the overall PCEs of the OPV devices. Electrical characterization results revealed that the presence of the metallic NPs had a negligible effect on the charge transport process, suggesting that the electrical properties were not sacrificed. Moreover, steady state and dynamic photoluminescence (PL) measurements provided strong evidence that the LSPR induced by the Au NPs not only increased the degree of light absorption but also enhanced the degree of exciton dissociation. As a result, the photocurrent and overall device efficiency were both improved considerably after exploiting the optical effects of the LSPR. Compared with previous approaches toward plasmonic-enhanced OPV devices, which involved the nanofabrication of plasmoic nanostructures,[24−26] the method we report herein is simpler (solution processable) and also suitable for the applications to the large-area processes.

RESULTS AND DISCUSSION

Photovoltaic Characteristics. We used solution-processable Au NPs to trigger the LSPR; the average particle size was *ca.* 45 ± 5 nm, estimated from a scanning electron microscopy (SEM) image (inset of Figure 1). The extinction spectrum of the Au NPs, determined using UV–vis spectroscopy, is displayed in Figure 1. The resonance of the Au NPs in solution was located at *ca.* 550 nm. The plasmonic resonance regime of the Au NPs was close to the absorption peak of the P3HT/PCBM blends, thereby suggesting enhanced light-harvesting efficiency. Figure 2a displays the architecture of our plasmonic-enhanced OPV devices. The presence of Au NPs embedded in the anodic buffer layer was evident from the SEM images recorded for the modified (Figure 2c) and pristine (Figure 2b) poly(3,4-ethylenedioxythiophene):poly(styrene sulfonate) (PEDOT:PSS) layers. Notably, the distribution of the Au NPs (white dots) in the modified PEDOT:PSS layer was uniform; we observed no apparent aggregation between the Au NPs in the film prepared using this simple method.

Figure 3a displays the representative current density–voltage (*J*–*V*) characteristics, recorded under
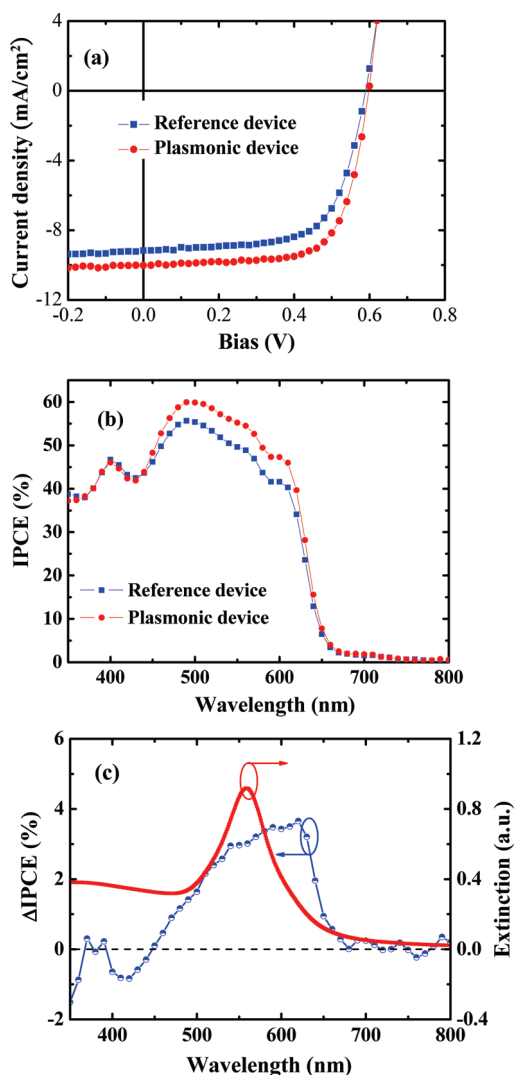
Figure 3. (a) $J–V$ characteristics, recorded under illumination at 100 mW cm^{-2} (AM 1.5G), of polymer solar cells with (plasmonic device) and without (reference device) Au NPs in the PEDOT:PSS layer. (b) Corresponding IPCE curves of these OPV devices. (c) Comparison between the curve of the increase in IPCE (ΔIPCE) after incorporating Au NPs and the extinction spectrum of the Au NPs.

Figure 4. (a) Photocurrent density (J_{ph}) plotted with respect to effective bias (V_{eff}) for the reference and plasmonic devices. (b) Exciton dissociation probability [$P(E,T)$] plotted with respect to effective bias (V_{eff}) for these OPV devices. The dissociation probabilities for the reference and plasmonic devices under short-circuit conditions were 78.2 and 84.2%, respectively.

100 mW cm^{-2} illumination (AM 1.5G), of OPV devices prepared using buffer layers with and without Au NPs. The reference device possessing the structure ITO/PEDOT:PSS/P3HT:PCBM/Ca/Al exhibited characteristics comparable to those of previously reported devices,[20,29] with an open-circuit voltage (V_{oc}) of 0.59 V, a short-circuit current (J_{sc}) of 9.16 mA cm^{-2}, and a fill factor (FF) of 66.06%, resulting in a PCE of 3.57%. To take advantage of the unique optical properties of the LSPR, we blended the Au NPs into the anodic buffer layer (denoted herein as the "plasmonic device"). The value of V_{oc} for the plasmonic device remained at 0.59 V, suggesting the unchanged nature of the electrode–organics interface. In contrast, the values of J_{sc} and FF both increased, to 10.22 mA cm^{-2} and 70.32%, respectively. Notably, the device resistance, extracted from the $J–V$ curves in the dark, increased
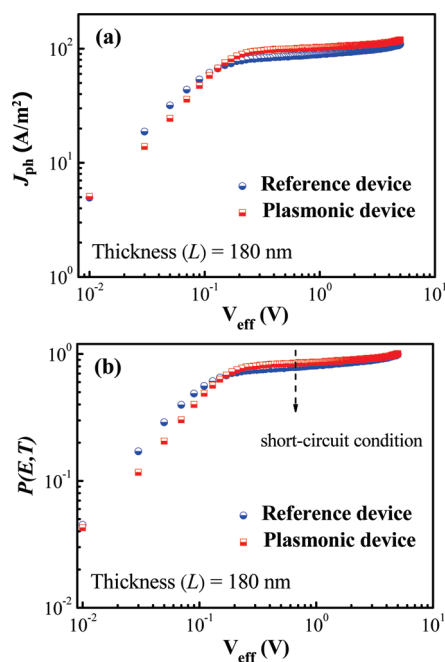
slightly from 1.79 to 1.82 $\Omega \cdot$cm^2 after incorporating the Au NPs. This potential drawback was, however, overwhelmed by the advantageous plasmonic effects. Overall, the plasmonic device's PCE was 4.24%.

Figure 3b presents incident photon-to-electron conversion efficiency (IPCE) curves for these devices. We also compared the curve of the increase in IPCE (ΔIPCE) after incorporating Au NPs with the extinction spectrum of the Au NPs (Figure 3c). The photocurrent within the wavelength range from 450 to 650 nm increased significantly after incorporating the Au NPs. This wavelength regime coincides with the extinction range of the Au NPs, indicating that LSPR effects did indeed improve the photocurrent.

Photocurrent Behavior. To further explore the effects of LSPR in OPV devices, we determined the maximum exciton generation rate (G_{max}). The devices were biased sweeping from $+1$ to -10 V. Figure 4a reveals the dependence of the photocurrent density (J_{ph}) on the effective voltage (V_{eff}), recorded under illumination at 100 mW cm^{-2}, for our reference and plasmonic devices. Here

$$J_{ph} = J_L - J_D$$

where J_L and J_D are the current densities under illumination and in the dark, respectively, and

$$V_{eff} = V_o - V_a$$

where V_o is the voltage when J_{ph} equals zero (i.e., $J_L = J_D$) and V_a is the applied voltage. Apparently, J_{ph}
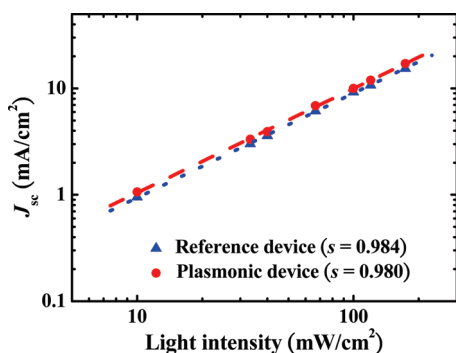
Figure 5. Values of J_{sc} of the OPVs plotted with respect to the light intensity. Straight lines were fitted using the expression $J_{sc} \propto P_{light}{}^s$; the values of s for the reference and plasmonic devices were 0.984 and 0.980, respectively.

linearly increased with the voltage at a low value of V_{eff} and then saturated at a sufficiently high value of V_{eff}. From Figure 4a, we therefore determined the values of the saturation photocurrent density (J_{sat}), which is independent of the bias and temperature. Furthermore, assuming that all of the photogenerated excitons dissociated and contributed to the current in the saturated regime due to the sufficiently high electric field, we obtained the values of G_{max} using the equation

$$J_{sat} = qG_{max}L$$

where q is the electronic charge and L is the thickness of the active layer.[5,33] The values of G_{max} for the reference and plasmonic devices were 3.96×10^{27} m^{-3} s^{-1} (J_{sat} = 114 A m^{-2}) and 4.27×10^{27} m^{-3} s^{-1} (J_{sat} = 123 A m^{-2}), respectively. Thus, a noticeable enhancement in G_{max} occurred after incorporating the Au NPs into the device. Because the value of G_{max} is a measure of the maximum number of photons absorbed,[5,33] such an increase suggests enhanced light absorption in the active layer of the plasmonic device.

Next, we compared the exciton dissociation probabilities [$P(E,T)$], which are related to the electric field (E) and temperature (T), for our devices. For OPVs, when the excitons are photogenerated, only a portion of them can be dissociated into free carriers. As a result, J_{ph} can be expressed using the equation[5,33]

$$J_{ph} = qG_{max}P(E, T)L$$

As a result, the value of $P(E,T)$ at any bias can be obtained from the plot of the normalized photocurrent density (J_{ph}/J_{sat}) with respect to V_{eff}.[34] Figure 4b reveals that the value of $P(E,T)$ under the short-circuit conditions (V_a = 0 V) increased from 79.2% for the reference device to 84.4% for the plasmonic device, indicating that excitation of the LSPR also facilitated excitons to dissociate into free carriers. Thus, excitation of the LSPR increased both the exciton generation rate and the dissociation probability, thereby enhancing the photocurrent of the OPVs.

Charge Transport Behavior. We measured the values of J_{sc} of our OPV devices at various illumination intensities to examine how the plasmonic effects influenced the charge transport process. Figure 5 displays the dependence of the incident light intensity (P_{light}) on the photocurrent. In general, the value of J_{sc} of an OPV device follows a power-law dependence with respect to P_{light} (*i.e.*, $J_{sc} \propto P_{light}{}^s$).[5,10] From Figure 5, we determined exponential factors (s) for the reference and plasmonic devices of 0.984 and 0.980, respectively. The nearly linear dependence of J_{sc} on the incident light intensity suggests the absence of bimolecular recombination and space-limited charges in either of these devices.[5,10] Therefore, we suspect that the incorporation of Au NPs into the buffer layer had a negligible influence on the nature of the charge transport process in the device. More importantly, however, the resulting plasmonic effects resulted in unique optical properties that improved the performance of the OPV devices.

Steady State Photoluminescence. To explore the effect of the LSPR on the exciton generation behavior, we performed steady state PL measurements. Because absorption in the donor phase (*i.e.*, P3HT) contributed predominately to the exciton generation in the active blend, we recorded fluorescence spectra of the pristine P3HT films. The samples were prepared by spin-coating pristine P3HT films onto the PEDOT:PSS buffer layers in the presence and absence of the Au NPs. Figure 6 presents the room temperature PL spectra obtained using different wavelength excitation sources (λ_{exc} = 470 and 532 nm) for the reference and plasmonic samples. The integrating PL intensity of the plasmonic sample was enhanced by *ca.* 12 and 20% with respect to the reference sample when we excited the sample at 470 and 532 nm, respectively; these excitation wavelengths were selected intentionally to be located within the resonance regime of the LSPR (see Figure 1). The fluorescence process is dependent on the light excitation rate and the quantum yield, which is dependent on competition between the radiative and nonradiative decaying mechanisms.[35] Because the resonance frequency of the Au NPs was close to the absorption band of P3HT, we attribute the enhanced PL intensity to the fact that excitation of the LSPR increased the degree of light absorption and, thereby, enhanced the light excitation rate. This hypothesis is consistent with our measured device characteristics—namely, the greater value of G_{max} for the plasmonic device relative to that of the reference device. Consequently, the PL measurements suggested that, upon excitation of the LSPR, the enhanced excitation rate increased the density of photogenerated excitons in P3HT, thereby enhancing the fluorescence intensity.[36,37] Notably, another possible factor responsible for the enhanced PL intensity was related to the modification of excitonic states of P3HT due to
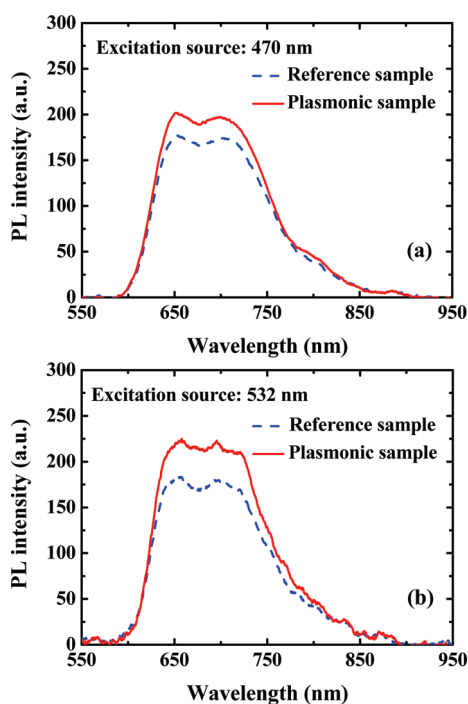
Figure 6. PL spectra of the reference and plasmonic samples recorded using excitation source wavelengths (λ_{exc}) of (a) 470 and (b) 532 nm.
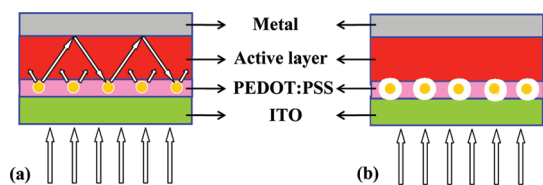

Figure 7. (a) Schematic representation of light trapping through forward scattering as a result of Au NP induced LSPR. The optical path length increased because light was trapped through multiple and high-angle scattering. (b) Schematic representation of the local enhancement of the electromagnetic field. The plasmonic field decays exponentially with respect to the distance from the surface of the Au NPs.

the presence of Au NPs.[31] This therefore accounted for the occurrence of the strong interactions between plasmonic field and excitons.

Our observation that LSPR enhanced the light absorption efficiency might result from two possible factors. First, the forward scattering lengthened the optical path in the active layer, thereby enhancing the degree of light absorption, as illustrated schematically in Figure 7a. Alternatively, excitation of the LSPR resulted in local enhancement of the electromagnetic field in the vicinity of the Au NPs (see Figure 7b); enhancement factors of up to 100 can be achieved.[38,39] Therefore, the resulting local field enhancement increased the total number of excitons created in the active layer because the energy dissipation is proportional to the intensity of the electromagnetic field.[40,41] For plasmonic metallic NPs, however, the particle size
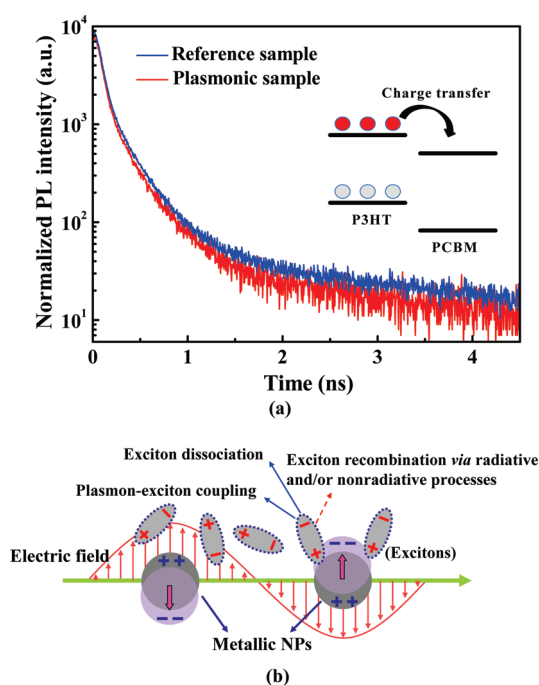

Figure 8. (a) PL decay profiles for the P3HT/PCBM blends in the reference and plasmonic samples. Excitation source: 470 nm pulsed laser. Inset: Schematic representation of the charge transfer process in the P3HT/PCBM blend. For the reference and plasmonic samples, the values of τ_{exciton} were 0.36 and 0.27 ns, respectively. (b) Cartoon depiction of the interplay between the LSPR and the excitons. The resulting interactions enhanced the rate of exciton dissociation, thereby reducing exciton recombination.

plays an important role in dominating the extinction behavior (*e.g.*, the sum of light absorption and scattering). Light scattering, which is beneficial for collecting light in inorganic solar cells,[42,43] becomes more dominant when using larger NPs. Typically, the light scattering efficiency is lower than the light absorption efficiency for Au NPs having particle sizes of less than 100 nm.[42,44] Because the average particle size of the Au NPs used in this study was only 45 nm, they were presumably unable to induce efficient light scattering. Therefore, we conclude that the LSPR effects, induced by the presence of the Au NPs, enhanced light collection in the active layer of OPVs predominately through local field enhancement.

Dynamic Photoluminescence. We employed time-resolved PL spectroscopy to acquire insight into the coupling process between the plasmonic field and the photogenerated excitons within the photoactive blend. Through measurements of exciton lifetimes (τ_{exciton}), the dynamic PL signal allowed us to probe how the plasmonic effects influenced the photophysical processes between the donor and acceptor phases.[45–47] Figure 8a displays the PL intensity decay profiles, obtained using a 470 nm excitation source, of P3HT/PCBM films that had been deposited on PEDOT:PSS layers in the presence and absence of Au NPs. The PL decay data were fitted using the following
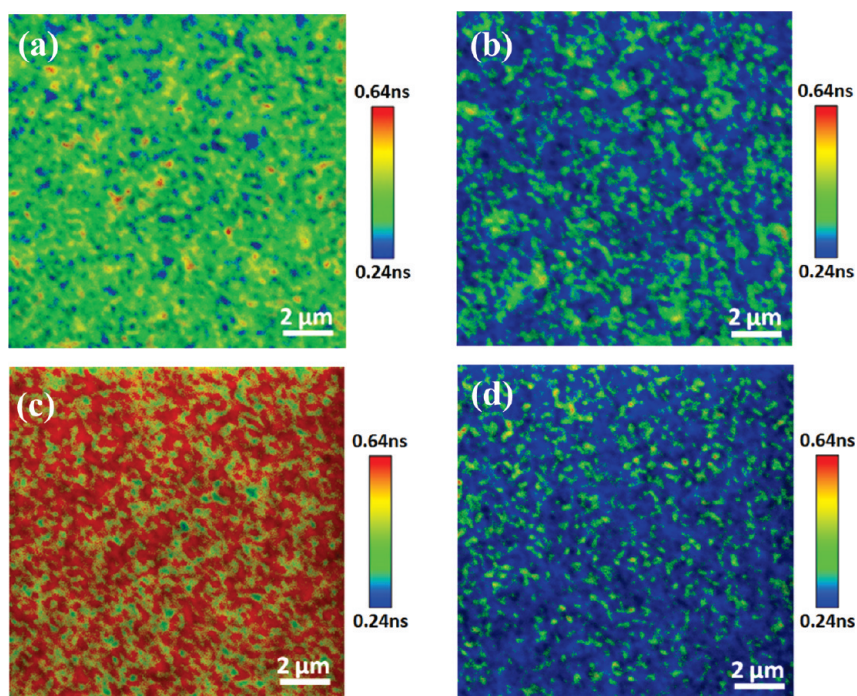
Figure 9. Exciton lifetime images for the reference (a,c) and plasmonic (b,d) samples. (a,b) Positions away from the PEDOT:PSS layer; (c,d) positions close to the PEDOT:PSS layer.

multiexponential function:[48]

$$I_{PL}(t) = \sum_{i=1}^{n} A_i \exp\left(-\frac{t}{\tau_i}\right) \qquad (1)$$

where A_i is the amplitude of the ith decay, n is the number of decays involved, and τ_i is the ith exponential constant. For the reference sample, we used two exponential constants (τ_1 and τ_2) to obtain a good fit to the data; their values of 0.200 and 0.558 ns, respectively, provided a corresponding value of $\tau_{exciton}$ of 0.36 ns. For the plasmonic sample, however, we required a third exponential constant (τ_3) to obtain a better fit; the values of these three exponential constants were 0.131, 0.324, and 0.015 ns, respectively, providing a resulting lower value of $\tau_{exciton}$ of 0.27 ns. Note that the introduction of τ_3 was necessary presumably because of the presence of the LSPR, which interacted with photogenerated excitons.

The dramatic change in the value of $\tau_{exciton}$ after incorporating Au NPs also accounted for the presence of the strong coupling between the plasmonic field and excitons, which has been reported previously.[31,49,50] We speculated that the resulting plasmon−exciton coupling participated in the charge transfer process, thus facilitating exciton dissociation, as illustrated in Figure 8b. The photophysical process can be further interpreted by the concept of "*hot excitons*" which possess excess energy to overcome their initial Coulombic potential.[31,49,50] Therefore, the generation of hot excitons is beneficial for enhancing the probability of dissociation into free polarons.[31,49,50] Previous reports have shown that the plasmonic field can strongly modify the dynamic properties of photogenerated excitons through the plasmon−exciton coupling.[51,52] This phenomenon presumably increased the amount of hot excitons for efficient dissociation.[31] As a result, the enhanced degree of exciton dissociation reduced the recombination level of geminate excitons through radiative and/or nonradiative processes and, thereby, improved the FFs of OPVs.[53,54] Note that the device resistance for the plasmonic device increased slightly relative to that of the reference device; therefore, it was not responsible for the enhanced FF. Consequently, we assigned the increased FF observed in Figure 3a primarily to the increased value of $P(E,T)$ resulting from the interplay between the plasmonic field and the photogenerated excitons.

We performed exciton lifetime mapping by combining the time-resolved PL measurement system with confocal laser scanning microscopy to further investigate the plasmonic effects.[45,47] This technique enabled us to examine the distribution of the exciton lifetimes on any given z-axial planes (close to or away from the PEDOT:PSS layer, in which the Au NPs were embedded). As a result, we could obtain the vertical evolution of $\tau_{exciton}$ in the P3HT/PCBM films. Figure 9 displays the exciton lifetime images (15 μm $\times$ 15 μm) for the reference and plasmonic samples (P3HT/PCBM films). The values of $\tau_{exciton}$, both close to or away from the PEDOT:PSS layer, generally decreased after incorporating the Au NPs. To quantify the average values and distributions of the exciton lifetimes, we constructed the corresponding statistical histograms for these
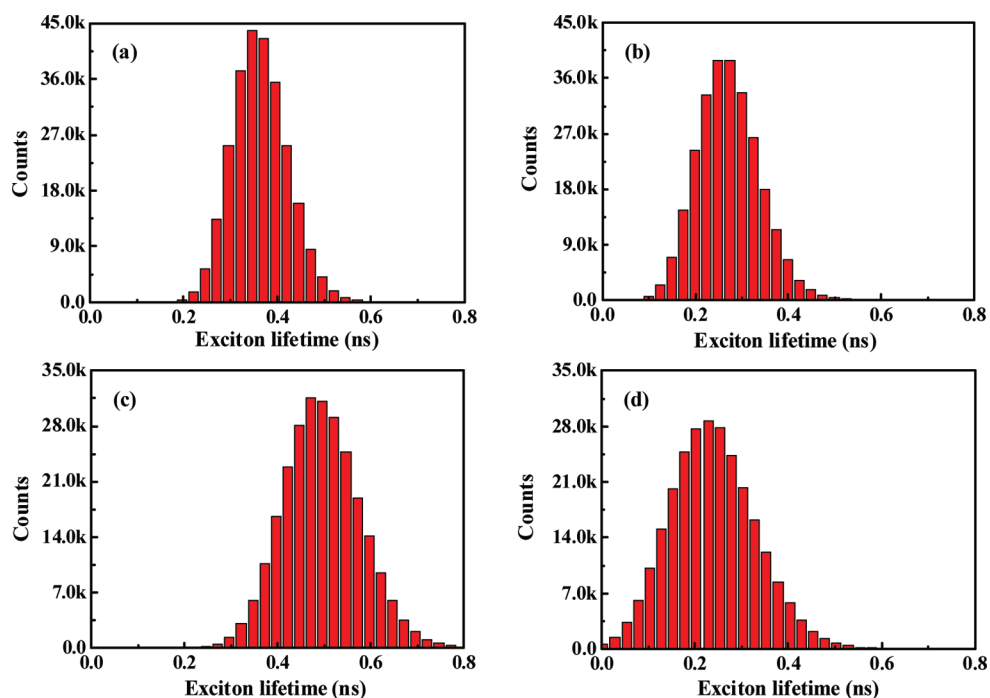
Figure 10. Histograms corresponding to the exciton lifetime images in Figure 9. Average values of $\tau_{exciton}$: (a) 0.35, (b) 0.27, (c) 0.48, and (d) 0.23 ns.

samples. For the reference sample, the average value of $\tau_{exciton}$ decreased from 0.48 ns close to the PEDOT:PSS layer (Figure 10c) to 0.35 ns away from the PEDOT:PSS layer (Figure 10a), presumably because the difference between the surface energies of P3HT and PCBM resulted in an inhomogeneous distribution of PCBM molecules in the P3HT matrix when the blend underwent solvent annealing.[45] The average values of $\tau_{exciton}$ decreased significantly (to 0.27 and 0.23 in panels b and d in Figure 10, respectively) after incorporating the Au NPs; notably, the average value of $\tau_{exciton}$ at the position close to the PEDOT:PSS layer was even lower than that away from the PEDOT:PSS layer. Therefore, for the plasmonic sample, we observed a reverse trend in the evolution of $\tau_{exciton}$. This result is not surprising because the plasmonic field decays exponentially with respect to the distance from the surface of the metallic NPs.[55,56] Therefore, stronger interplay between the plasmonic field and excitons occurred at positions close to the PEDOT:PSS layer, due to the localized enhanced near field in the proximity of the Au NPs. Notably, the time-resolved PL measurement data, in which LSPR changed the lifetime of the excitons in the active blend, further support the field enhancement

mechanism that we proposed above because we would not expect the scattering scheme to influence the exciton lifetime significantly.

CONCLUSIONS

Efficient light absorption in thin film solar cells is critical for their high performance—especially for those based on organic materials, where the thickness of the active layer is relatively thin. In this study, we improved the device PCEs of OPVs by incorporating Au NPs in the PEDOT:PSS buffer layer. The degree of light absorption in the plasmonic-enhanced OPV device increased significantly as a result of LSPR-induced local field enhancement. Moreover, interactions between the plasmons and the photogenerated excitons resulted in an enhanced degree of exciton dissociation, thereby reducing the level of exciton loss through geminate recombination. Without sacrificing the electrical properties, the incorporation of the Au NPs allowed the unique optical properties of the LSPR to improve the performance of the OPV. We believe that the results of this study might pave the way toward higher-efficiency OPV devices, and that this approach might also be applicable to systems featuring other types of active materials.

METHODS

Device Fabrication. The OPV device was fabricated on an indium tin oxide (ITO)-coated glass substrate. After a routine cleaning process, the substrate was dried overnight in an oven

and treated with UV ozone prior to use. To prepare the composite buffer layer, a Au NP solution was blended into the PEDOT:PSS (Baytron 4071) solution; the doping concentration of Au NPs inside the PEDOT:PSS solution was *ca.* 2×10^{11} cm^{-3}.

The Au NP solution was prepared using procedures described previously.[57] The anodic buffer layer was deposited through spin-coating onto a ITO-coated glass substrate and then thermally annealed at 120 °C for 1 h. To reduce the surface roughness of the composite buffer layer, an additional thinner layer of PEDOT:PSS was spin-coated as a capping layer. For comparison, the thickness of each buffer layer was set at *ca.* 50 nm. In a nitrogen-filled glovebox, a solution of P3HT (Rieke Metals) and PCBM (Solenne) dissolved (each at 17 mg mL^{-1}) in 1,2-dichlorobenzene (DCB) was spin-coated on top of the buffer layer. The wet film was subjected to solvent annealing in a glass Petri dish,[6] followed by a thermal annealing at 110 °C for 15 min. The thickness of the resulting photoactive layer was *ca.* 180 nm. To complete the device, a cathode (30 nm Ca and 100 nm Al) was deposited through thermal evaporation under a vacuum of *ca.* 6×10^{-6} Torr. The device area, defined through a shadow mask, was 0.12 cm^2. The completed device was encapsulated with a cover glass and sealed with a UV-curing epoxy resin prior to device testing.

Characterization. The *J*−*V* characteristics of the devices were measured using a Keithley 2400 source measure unit. The photocurrent response was obtained under illumination from a 150 W Thermal Oriel solar simulator (AM 1.5G). The illumination intensity was calibrated using a standard Si photodiode equipped with a KG-5 filter (Hamamatsu).[58] The IPCE measurement system (Enli Technology) comprised a quartz−tungsten−halogen (QTH) lamp as the light source, a monochromator, an optical chopper, a lock-in amplifier, and a calibrated silicon photodetector. The light intensity dependence study was conducted using neutral density filters to tune the light intensity. The dimensions of the Au NPs were measured using a JEOL JSM-7000F scanning electron microscope. Absorption spectra were measured using an UV/vis/near-IR spectrometer (PerkinElmer Lambda 950). The steady state PL spectra were recorded in the transmission mode under air ambient conditions; continuous-wave (CW) lasers (470 and 532 nm) were used as the excitation sources. The fluorescence emission signal was measured using a high-resolution spectrometer (HR4000, Ocean Optics). For the time-resolved PL measurements, the samples were excited using a 470 nm pulsed laser; the dynamic signal was recorded using a time-correlated single photon counting (TCSPC) spectrometer (LDH-P-C-470, Picoquant). For mapping of exciton lifetime images, the confocal laser scanning microscope (FV300, Olympus Corporation) was equipped with a single photon avalanche diode detector (PDM series, Picoquant).

REFERENCES AND NOTES

1. Chen, H. Y.; Hou, J. H.; Zhang, S. Q.; Liang, Y. Y.; Yang, G. W.; Yang, Y.; Yu, L. P.; Wu, Y.; Li, G. Polymer Solar Cells with Enhanced Open-Circuit Voltage and Efficiency. *Nat. Photonics* **2009,** *3,* 649–653.

2. Hou, J. H.; Chen, H. Y.; Zhang, S. Q.; Chen, R. I.; Yang, Y.; Wu, Y.; Li, G. Synthesis of a Low Band Gap Polymer and Its Application in Highly Efficient Polymer Solar Cells. *J. Am. Chem. Soc.* **2009,** *131,* 15586–15587.

3. Park, S. H.; Roy, A.; Beaupre, S.; Cho, S.; Coates, N.; Moon, J. S.; Moses, D.; Leclerc, M.; Lee, K.; Heeger, A. J. Bulk Heterojunction Solar Cells with Internal Quantum Efficiency Approaching 100%. *Nat. Photonics* **2009,** *3,* 297–303.

4. Liang, Y. Y.; Xu, Z.; Xia, J. B.; Tsai, S. T.; Wu, Y.; Li, G.; Ray, C.; Yu, L. P. For the Bright Future─Bulk Heterojunction Polymer Solar Cells with Power Conversion Efficiency of 7.4%. *Adv. Mater.* **2010,** *22,* E135–E138.

5. Mihailetchi, V. D.; Xie, H. X.; de Boer, B.; Koster, L. J. A.; Blom, P. W. M. Charge Transport and Photocurrent Generation in Poly(3-hexylthiophene):Methanofullerene Bulk-Heterojunction Solar Cells. *Adv. Funct. Mater.* **2006,** *16,* 699–708.

6. Li, G.; Shrotriya, V.; Huang, J. S.; Yao, Y.; Moriarty, T.; Emery, K.; Yang, Y. High-Efficiency Solution Processable Polymer Photovoltaic Cells by Self-Organization of Polymer Blends. *Nat. Mater.* **2005,** *4,* 864–868.

7. Sariciftci, N. S.; Smilowitz, L.; Heeger, A. J.; Wudl, F. Photoinduced Electron-Transfer from a Conducting Polymer to Buckminsterfullerene. *Science* **1992,** *258,* 1474–1476.

8. Yu, G.; Gao, J.; Hummelen, J. C.; Wudl, F.; Heeger, A. J. Polymer Photovoltaic Cells. Enhanced Efficiencies via a Network of Internal Donor−Acceptor Heterojunctions. *Science* **1995,** *270,* 1789–1791.

9. Jo, J.; Na, S. I.; Kim, S. S.; Lee, T. W.; Chung, Y.; Kang, S. J.; Vak, D.; Kim, D. Y. Three-Dimensional Bulk Heterojunction Morphology for Achieving High Internal Quantum Efficiency in Polymer Solar Cells. *Adv. Funct. Mater.* **2009,** *19,* 2398–2406.

10. Schilinsky, P.; Waldauf, C.; Brabec, C. J. Recombination and Loss Analysis in Polythiophene Based Bulk Heterojunction Photodetectors. *Appl. Phys. Lett.* **2002,** *81,* 3885–3887.

11. Shrotriya, V.; Wu, E. H. E.; Li, G.; Yao, Y.; Yang, Y. Efficient Light Harvesting in Multiple-Device Stacked Structure for Polymer Solar Cells. *Appl. Phys. Lett.* **2006,** *88,* 064104.

12. Yakimov, A.; Forrest, S. R. High Photovoltage Multiple-Heterojunction Organic Solar Cells Incorporating Interfacial Metallic Nanoclusters. *Appl. Phys. Lett.* **2002,** *80,* 1667–1669.

13. Chen, F. C.; Wu, J. L.; Hung, Y. Spatial Redistribution of the Optical Field Intensity in Inverted Polymer Solar Cells. *Appl. Phys. Lett.* **2010,** *96,* 193304.

14. Gilot, J.; Barbu, I.; Wienk, M. M.; Janssen, R. A. J. The Use of ZnO as Optical Spacer in Polymer Solar Cells: Theoretical and Experimental Study. *Appl. Phys. Lett.* **2007,** *91,* 113520.

15. Kim, J. Y.; Kim, S. H.; Lee, H. H.; Lee, K.; Ma, W. L.; Gong, X.; Heeger, A. J. New Architecture for High-Efficiency Polymer Photovoltaic Cells Using Solution-Based Titanium Oxide as an Optical Spacer. *Adv. Mater.* **2006,** *18,* 572–576.

16. Roy, A.; Park, S. H.; Cowan, S.; Tong, M. H.; Cho, S. N.; Lee, K.; Heeger, A. J. Titanium Suboxide as an Optical Spacer in Polymer Solar Cells. *Appl. Phys. Lett.* **2009,** *95,* 013302.

17. Tvingstedt, K.; Andersson, V.; Zhang, F.; Inganäs, O. Folded Reflective Tandem Polymer Solar Cell Doubles Efficiency. *Appl. Phys. Lett.* **2007,** *91,* 123514.

18. Zhou, Y. H.; Zhang, F. L.; Tvingstedt, K.; Tian, W. J.; Inganäs, O. Multifolded Polymer Solar Cells on Flexible Substrates. *Appl. Phys. Lett.* **2008,** *93,* 033302.

19. Cocoyer, C.; Rocha, L.; Sicot, L.; Geffroy, B.; de Bettignies, R.; Sentein, C.; Fiorini-Debuisschert, C.; Raimond, P. Implementation of Submicrometric Periodic Surface Structures toward Improvement of Organic-Solar-Cell Performances. *Appl. Phys. Lett.* **2006,** *88,* 133108.

20. Na, S. I.; Kim, S. S.; Jo, J.; Oh, S. H.; Kim, J.; Kim, D. Y. Efficient Polymer Solar Cells with Surface Relief Gratings Fabricated by Simple Soft Lithography. *Adv. Funct. Mater.* **2008,** *18,* 3956–3963.

21. Ko, D. H.; Tumbleston, J. R.; Zhang, L.; Williams, S.; DeSimone, J. M.; Lopez, R.; Samulski, E. T. Photonic Crystal Geometry for Organic Solar Cells. *Nano Lett.* **2009,** *9,* 2742–2746.

22. Tumbleston, J. R.; Ko, D. H.; Samulski, E. T.; Lopez, R. Absorption and Quasiguided Mode Analysis of Organic Solar Cells with Photonic Crystal Photoactive Layers. *Opt. Express* **2009,** *17,* 7670–7681.

23. Long, Y. B. Improving Optical Performance of Inverted Organic Solar Cells by Microcavity Effect. *Appl. Phys. Lett.* **2009,** *95,* 193301.

24. Kang, M. G.; Xu, T.; Park, H. J.; Luo, X.; Guo, L. J. Efficiency Enhancement of Organic Solar Cells Using Transparent Plasmonic Ag Nanowire Electrodes. *Adv. Mater.* **2010,** *22,* 4378–4383.

25. Lindquist, N. C.; Luhman, W. A.; Oh, S. H.; Holmes, R. J. Plasmonic Nanocavity Arrays for Enhanced Efficiency in Organic Photovoltaic Cells. *Appl. Phys. Lett.* **2008,** *93,* 123308.

26. Tvingstedt, K.; Persson, N. K.; Inganäs, O.; Rahachou, A.; Zozoulenko, I. V. Surface Plasmon Increase Absorption in

Polymer Photovoltaic Cells. *Appl. Phys. Lett.* **2007,** *91,* 123514.

27. Kim, S. S.; Na, S. I.; Jo, J.; Kim, D. Y.; Nah, Y. C. Plasmon Enhanced Performance of Organic Solar Cells Using Electrodeposited Ag Nanoparticles. *Appl. Phys. Lett.* **2008,** *93,* 073307.

28. Chang, Y. C.; Chou, F. Y.; Yeh, P. H.; Chen, H. W.; Chang, S. H.; Lan, Y. C.; Guo, T. F.; Tsai, T. C.; Lee, C. T. Effects of Surface Plasmon Resonant Scattering on the Power Conversion Efficiency of Organic Thin-Film Solar Cells. *J. Vac. Sci. Technol., B* **2007,** *25,* 1899–1902.

29. Chen, F. C.; Wu, J. L.; Lee, C. L.; Hong, Y.; Kuo, C. H.; Huang, M. H. Plasmonic-Enhanced Polymer Photovoltaic Devices Incorporating Solution-Processable Metal Nanoparticles. *Appl. Phys. Lett.* **2009,** *95,* 013305.

30. Morfa, A. J.; Rowlen, K. L.; Reilly, T. H.; Romero, M. J.; van de Lagemaat, J. Plasmon-Enhanced Solar Energy Conversion in Organic Bulk Heterojunction Photovoltaics. *Appl. Phys. Lett.* **2008,** *92,* 013504.

31. Lee, J. H.; Park, J. H.; Kim, J. S.; Lee, D. Y.; Cho, K. High Efficiency Polymer Solar Cells with Wet Deposited Plasmonic Gold Nanodots. *Org. Electron.* **2009,** *10,* 416–420.

32. Kulkarni, A. P.; Noone, K. M.; Munechika, K.; Guyer, S. R.; Ginger, D. S. Plasmon-Enhanced Charge Carrier Generation in Organic Photovoltaic Films Using Silver Nanoprisms. *Nano Lett.* **2010,** *10,* 1501–1505.

33. Mihailetchi, V. D.; Koster, L. J. A.; Hummelen, J. C.; Blom, P. W. M. Photocurrent Generation in Polymer−Fullerene Bulk Heterojunctions. *Phys. Rev. Lett.* **2004,** *93,* 216601.

34. Shrotriya, V.; Yao, Y.; Li, G.; Yang, Y. Effect of Self-Organization in Polymer/Fullerene Bulk Heterojunctions on Solar Cell Performance. *Appl. Phys. Lett.* **2006,** *89,* 063505.

35. Anger, P.; Bharadwaj, P.; Novotny, L. Enhancement and Quenching of Single-Molecule Fluorescence. *Phys. Rev. Lett.* **2006,** *96,* 113002.

36. Mahmoud, M. A.; Poncheri, A. J.; Phillips, R. L.; El-Sayed, M. A. Plasmonic Field Enhancement of the Exciton−Exciton Annihilation Process in a Poly(*p*-phenyleneethynylene) Fluorescent Polymer by Ag Nanocubes. *J. Am. Chem. Soc.* **2010,** *132,* 2633–2641.

37. Konda, R. B.; Mundle, R.; Mustafa, H.; Bamiduro, O.; Pradhana, A. K.; Roy, U. N.; Cui, Y.; Burger, A. Surface Plasmon Excitation *via* Au Nanoparticles in n-CdSe/p-Si Heterojunction Diodes. *Appl. Phys. Lett.* **2007,** *91,* 191111.

38. Maier, S. A.; Atwater, H. A. Plasmonics: Localization and Guiding of Electromagnetic Energy in Metal/Dielectric Structures. *J. Appl. Phys.* **2005,** *98,* 011101.

39. Rand, B. P.; Peumans, P.; Forrest, S. R. Long-Range Absorption Enhancement in Organic Tandem Thin-Film Solar Cells Containing Silver Nanoclusters. *J. Appl. Phys.* **2004,** *96,* 7519–7526.

40. Monestier, F.; Simon, J. J.; Torchio, P.; Escoubas, L.; Florya, F.; Bailly, S.; de Bettignies, R.; Guillerez, S.; Defranoux, C. Modeling the Short-Circuit Current Density of Polymer Solar Cells Based on P3HT:PCBM Blend. *Sol. Energy Mater. Sol. Cells* **2007,** *91,* 405–410.

41. Pettersson, L. A. A.; Roman, L. S.; Inganäs, O. Modeling Photocurrent Action Spectra of Photovoltaic Devices Based on Organic Thin Films. *J. Appl. Phys.* **1999,** *86,* 487–496.

42. Derkacs, D.; Lim, S. H.; Matheu, P.; Mar, W.; Yu, E. T. Improved Performance of Amorphous Silicon Solar Cells *via* Scattering from Surface Plasmon Polaritons in Nearby Metallic Nanoparticles. *Appl. Phys. Lett.* **2006,** *89,* 093103.

43. Derkacs, D.; Chen, W. V.; Matheu, P. M.; Lim, S. H.; Yu, P. K. L.; Yu, E. T. Nanoparticle-Induced Light Scattering for Improved Performance of Quantum-Well Solar Cells. *Appl. Phys. Lett.* **2008,** *93,* 091107.

44. van Dijk, M. A.; Tchebotareva, A. L.; Orrit, M.; Lippitz, M.; Berciaud, S.; Lasne, D.; Cognet, L.; Lounis, B. Absorption and Scattering Microscopy of Single Metal Nanoparticles. *Phys. Chem. Chem. Phys.* **2006,** *8,* 3486–3495.

45. Huang, J. H.; Chien, F. C.; Chen, P. L.; Ho, K. C.; Chu, C. W. Monitoring the 3D Nanostructures of Bulk Heterojunction Polymer Solar Cells Using Confocal Lifetime Imaging. *Anal. Chem.* **2010,** *82,* 1669–1673.

46. Huang, J. H.; Yang, C. Y.; Ho, Z. Y.; Kekuda, D.; Wu, M. C.; Chien, F. C.; Chen, P. L.; Chu, C. W.; Ho, K. C. Annealing Effect of Polymer Bulk Heterojunction Solar Cells Based on Polyfluorene and Fullerene Blend. *Org. Electron.* **2009,** *10,* 27–33.

47. Huang, J. H.; Li, K. C.; Chien, F. C.; Hsiao, Y. S.; Kekuda, D.; Chen, P.; Lin, H. C.; Ho, K. C.; Chu, C. W. Corrrelation between Exciton Lifetime Distribution and Morphology of Bulk Heterojunction Films after Solvent Annealing *J. Phys. Chem. C* **2010,** *114,* 9062–9069.

48. Jones, M.; Nedeljkovic, J.; Ellingson, R. J.; Nozik, A. J.; Rumbles, G. Photoenhancement of Luminescence in Colloidal CdSe Quantum Dot Solutions. *J. Phys. Chem. B* **2003,** *107,* 11346–11352.

49. Zhu, X. Y.; Yang, Q.; Muntwiler, M. Charge-Transfer Excitons at Organic Semiconductor Surfaces and Interfaces. *Acc. Chem. Res.* **2009,** *42,* 1779–1787.

50. Ohkita, H.; Cook, S.; Astuti, Y.; Duffy, W.; Tierney, S.; Zhang, W.; Heeney, M.; McCulloch, I.; Nelson, J.; Bradley, D. D. C.; *et al.* Charge Carrier Formation in Polythiophene/Fullerene Blend Films Studied by Transient Absorption Spectroscopy. *J. Am. Chem. Soc.* **2008,** *130,* 3030–3042.

51. Fofang, N. T.; Park, T. H.; Neumann, O.; Mirin, N. A.; Nordlander, P.; Halas, N. J. Plexcitonic Nanoparticles: Plasmon−Exciton Coupling in Nanoshell−J-Aggregate Complexes. *Nano Lett.* **2008,** *8,* 3481–3487.

52. Bellessa, J.; Bonnand, C.; Plenet, J. C. Strong Coupling between Surface Plasmons and Excitons in an Organic Semiconductor. *Phys. Rev. Lett.* **2004,** *93,* 036404.

53. Moet, D. J. D.; Lenes, M.; Morana, M.; Azimi, H.; Brabec, C. J.; Blom, P. W. M. Enhanced Dissociation of Charge-Transfer States in Narrow Band Gap Polymer:Fullerene Solar Cells Processed with 1,8-Octanedithiol. *Appl. Phys. Lett.* **2010,** *96,* 213506.

54. Mandoc, M. M.; Veurman, W.; Koster, L. J. A.; de Boer, B.; Blom, P. W. M. Origin of the Reduced Fill Factor and Photocurrent in MDMO-PPV:PCNEPV All-Polymer Solar Cells. *Adv. Funct. Mater.* **2007,** *17,* 2167–2173.

55. Lal, S.; Link, S.; Halas, N. J. Nano-Optics from Sensing to Waveguiding. *Nat. Photonics* **2007,** *1,* 641–648.

56. Barnes, W. L.; Dereux, A.; Ebbesen, T. W. Surface Plasmon Subwavelength Optics. *Nature* **2003,** *424,* 824–830.

57. Chang, C. C.; Wu, H. L.; Kuo, C. H.; Huang, M. H. Hydrothermal Synthesis of Monodispersed Octahedral Gold Nanocrystals with Five Different Size Ranges and Their Self-Assembled Structures. *Chem. Mater.* **2008,** *20,* 7570–7574.

58. Shrotriya, V.; Li, G.; Yao, Y.; Moriarty, T.; Emery, K.; Yang, Y. Accurate Measurement and Characterization of Organic Solar Cells. *Adv. Funct. Mater.* **2006,** *16,* 2016–2023.